Geophysical Journal International

Geophys. J. Int. (2018) **214,** 2151–2163
Advance Access publication 2018 June 23
GJI Seismology

doi: 10.1093/gji/ggy253

High *Vp*/*Vs* ratio in the crust and uppermost mantle beneath volcanoes in the Central and Eastern Anatolia

Hejun Zhu

Department of Geosciences, The University of Texas at Dallas, Richardson, Dallas 75080-3021*, TX. E-mail: hejun.zhu@utdallas.edu*

Accepted 2018 June 21. Received 2018 June 12; in original form 2017 August 23

SUMMARY

In this paper, I analyse *Vp*, *Vs* and *Vp*/*Vs* ratio for the crust and uppermost mantle of Anatolia in EU_{60}, a recently developed 3-D tomographic model for the European continent. Beneath volcanic fields in the Central and Eastern Anatolia, pronounced reductions in isotropic *Vs* are observed in the crust and uppermost mantle, reflecting high temperature associated with Neogene–Quaternary magmatism in the study region. These slow wave speed anomalies correlate well with high *Vp*/*Vs* ratio in model EU_{60}. By analysing relative perturbations in *Vp* and *Vs* at different depths, I observe a distinct pattern for grid points associated with volcanic and non-volcanic regions. The linear regression results of volcanic grid points are characterized by high $\delta \ln V_s / \delta \ln V_p$ slopes in comparison with non-volcanic grid points. Grid points with linear fitting slopes greater than 2.2 are observed around 50–60 km beneath volcanic provinces. These observations suggest the presence of partial melt in the crust and uppermost mantle beneath volcanoes in the Central and Eastern Anatolia. Comparisons between seismic observations with theoretical single phase partial melting calculations suggest the presence of cracks filled with a few volume per cent of melt in the upper and lower crust. Less than 1 per cent melt-filled inclusions with aspect ratio smaller than 0.001 might exist in the uppermost mantle.

Key words: Europe; Seismic tomography; Continental neotectonics.

1 INTRODUCTION

The Anatolian Plate is located along the Alpine–Himalayan orogenic belt. Its tectonic evolution involved complex interactions among surrounding plates, including the Eurasian, African and Arabian Plates (McKenzie 1972; Dewey *et al.* 1986). The recent tectonics of the Anatolian Plate is mainly controlled by the northward motion of the Arabian Plate, the westward extrusion and counterclockwise rotation of the Anatolian Plate (Reilinger *et al.* 1997), the Aegean trench retreat resulted from the slab rollback of the African Plate (Wortel & Spakman 2000). The counterclockwise rotation of the Anatolian Plate is accommodated by the North and East Anatolian Fault Zones (McKenzie 1972; Şengör *et al.* 1985), making the Anatolian Plate one of the most seismologically active regions in the world (Fig. 1).

Based on different deformation styles, Şengör *et al.* (1985) subdivided the Anatolian Plate into four major tectonic provinces: the East Anatolian contractional, the Central Anatolia, the North Anatolia and the Western Anatolian extensional province (Fig. 1a). The East Anatolian contractional province was created by young north–south continental collision between the Arabian Plate and the Eurasian Plate along the Bitlis–Zagros Suture Zone (BZSZ), leading to the uplift of the East Anatolian Plateau (EAP). Within the EAP, the young Miocene–Holocene Eastern Anatolian Volcanic Field (EAVF) spreads from the Arabian foreland basin to the Caucasus region. Isotope and trace element analysis suggested the source of this volcanism might be derived from the lower portion of the lithospheric mantle (Pearce *et al.* 1990). Geophysical surveys revealed thin lithosphere beneath the EAP (Sandvol *et al.* 1998; Ozacar *et al.* 2008). Some studies proposed that this active volcanism and the high elevation of the EAP (around 2 km) were produced by hot upwelling asthenosphere after the detachment of the subducting Arabian slab (Lei & Zhao 2007; Biryol *et al.* 2011). In addition, the EAP is characterized by reduced Bouguer gravity anomaly (Fig. 1c), reflecting its mass deficiency in comparison with surrounding regions (Ates *et al.* 1999). The Central Anatolia is bounded by the North Anatolian Fault (NAF) to the north and the East Anatolian Fault (EAF) to the southeast. In contrast to high elevation and reduced Bouguer gravity anomaly in the EAP, the Central Anatolia involves a flatter topography and moderate gravity anomaly. The central part of the Central Anatolia is characterized by several post-collision related volcanic fields, including the Central Anatolian Volcanic Field (CAVF) and the Kirka–Afyon–Isparta Volcanic Field (KAIVF; Fig. 1b). Geochemical signatures of basalt in the Central Anatolia suggested contributions from a subduction-related component and mantle asthenosphere (Reid *et al.* 2017). The North Anatolian province is dominated by right-lateral strike-slip motion along the NAF, which extends from the Karliova Triple Junction (KTJ) in the Eastern Anatolia to the Sea of Marmara. The NAF involves high seismic activity and recurrent major earthquakes

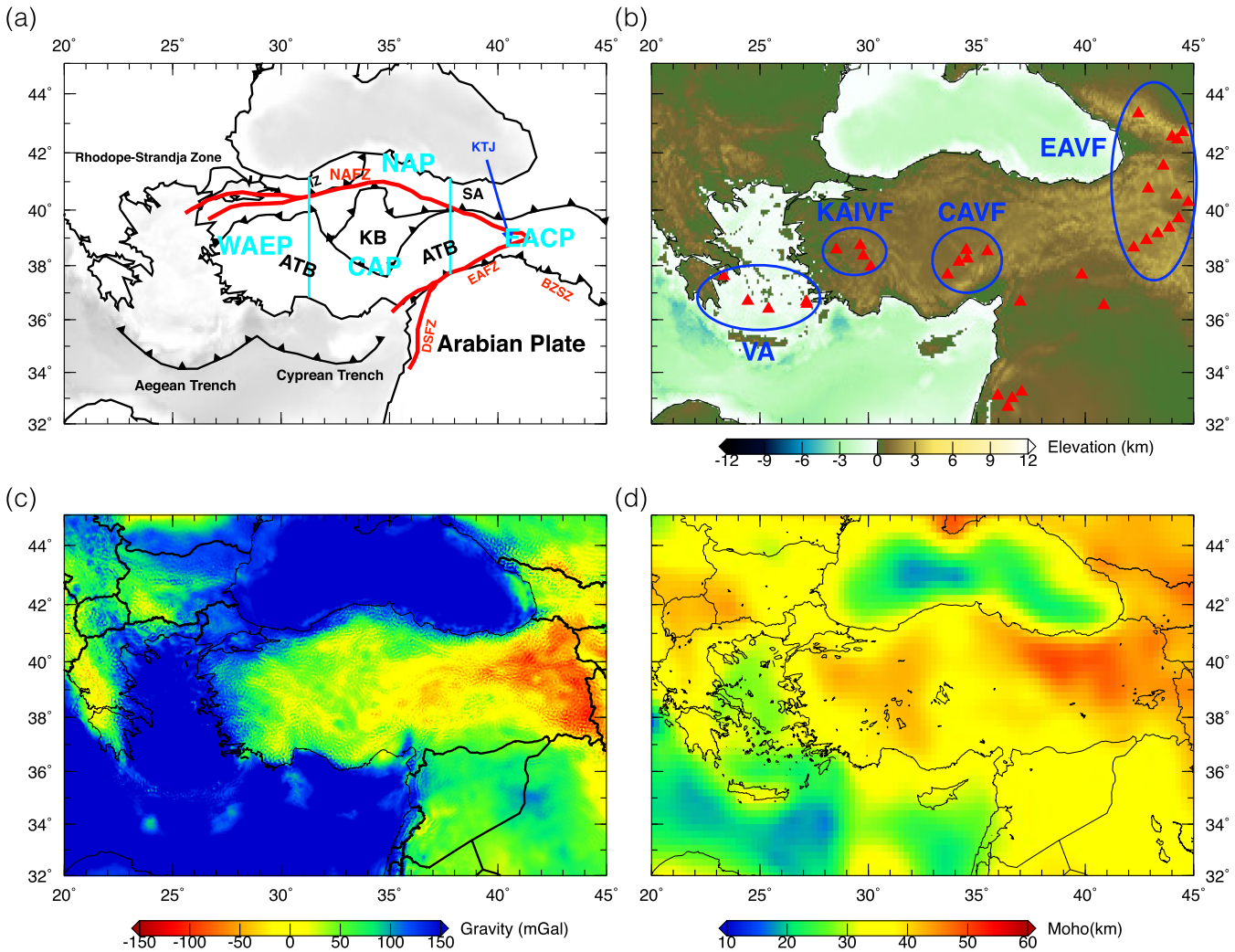

Figure 1. Geological map and geophysical measurements for the Anatolian Plate. Panel (a) shows a simplified geological map for the Anatolian Plate, modified from Delph *et al.* (2015). Blue vertical bars (from left to right) separate the Western Anatolian Extensional Province (WAEP), Central Anatolian Province (CAP) and Eastern Anatolian Contractional Province (EACP; Şengör *et al.* 1985). Red lines are fault zones in the study region: NAFZ, North Anatolian Fault Zone; EAFZ, East Anatolian Fault Zone; DSFZ, Dead Sea Fault Zone. Major tectonic structures include, ATB, Anatolide–Tauride Block; KB, Kirşehir Block; KTJ, Karliova Triple Junction; BZSZ, Bitlis-Zagros Suture Zone; IZ, Istanbul Zone. Panel (b) shows the distribution of volcanoes (red triangles) in Anatolia and Aegean. EAVF, Eastern Anatolian Volcanic Field; CAVF, Central Anatolian Volcanic Field; KAIVF, Kirka–Afyon–Isparta Volcanic Field; VA, Volcanic Arc. Panels (c) and (d) show Bouguer gravity anomaly from WGM2012 (http://bgi.omp.obs-mip.fr/data-products/Grids-and-models/wgm2012) and Moho depth from EPCrust (Molinari & Morelli 2011).

(M >7). The Western Anatolia is influenced by volcanic arcs along the Aegean Trench, which are related to the rollback of the African lithosphere over the past 15 Myr (Wortel & Spakman 2000).

Studying the subsurface signatures of the Anatolian volcanic fields enables us to better understand the magmatism and Neotectonics of the Anatolian Plate. In this paper, I use *Vp*, *Vs* and *Vp*/*Vs* results from a recently available tomographic model EU_{60} to detect potential partial melt beneath volcanic provinces in Anatolia. EU_{60} is a tomographic model for the entire European continent built based on adjoint tomography, an advanced imaging technique taking complicated wave physics into account, including wave front healing, finite-frequency and multipathing effects. It is closely related to full waveform inversion in exploration seismology (Lailly 1983; Tarantola 1984; Virieux & Operto 2009). In comparison to classical traveltime tomography, adjoint tomography enables us to better estimate seismic parameters in the subsurface, and produce high-resolution and high-fidelity tomographic images. Adjoint tomography has been utilized to simultaneously constrain subsurface variations in wave speeds, attenuation, as well as radial and azimuthal anisotropy (Zhu *et al.* 2013; Zhu & Tromp 2013). Jointly analysing these seismic parameters allows us to better interpret tomographic results and reduce ambiguity in inferring variations in physical factors, such as temperature, water content, partial melt and composition. For instance, joint interpretation of 3-D variations in *Vp*, *Vs* and *Vp*/*Vs* ratio allows us to detect the presence of partial melt, especially underneath volcanic areas, such as Japan (Nakajima *et al.* 2001) and Hawaii (Lin *et al.* 2015). In this study, I compare seismic observations with theoretically calculated *Vp* and *Vp*/*Vs* for a composite with melt-filled inclusions. These comparisons enable me to quantitatively estimate the amount of melt as well as the shape of inclusions beneath volcanoes in the Central and Eastern Anatolia.

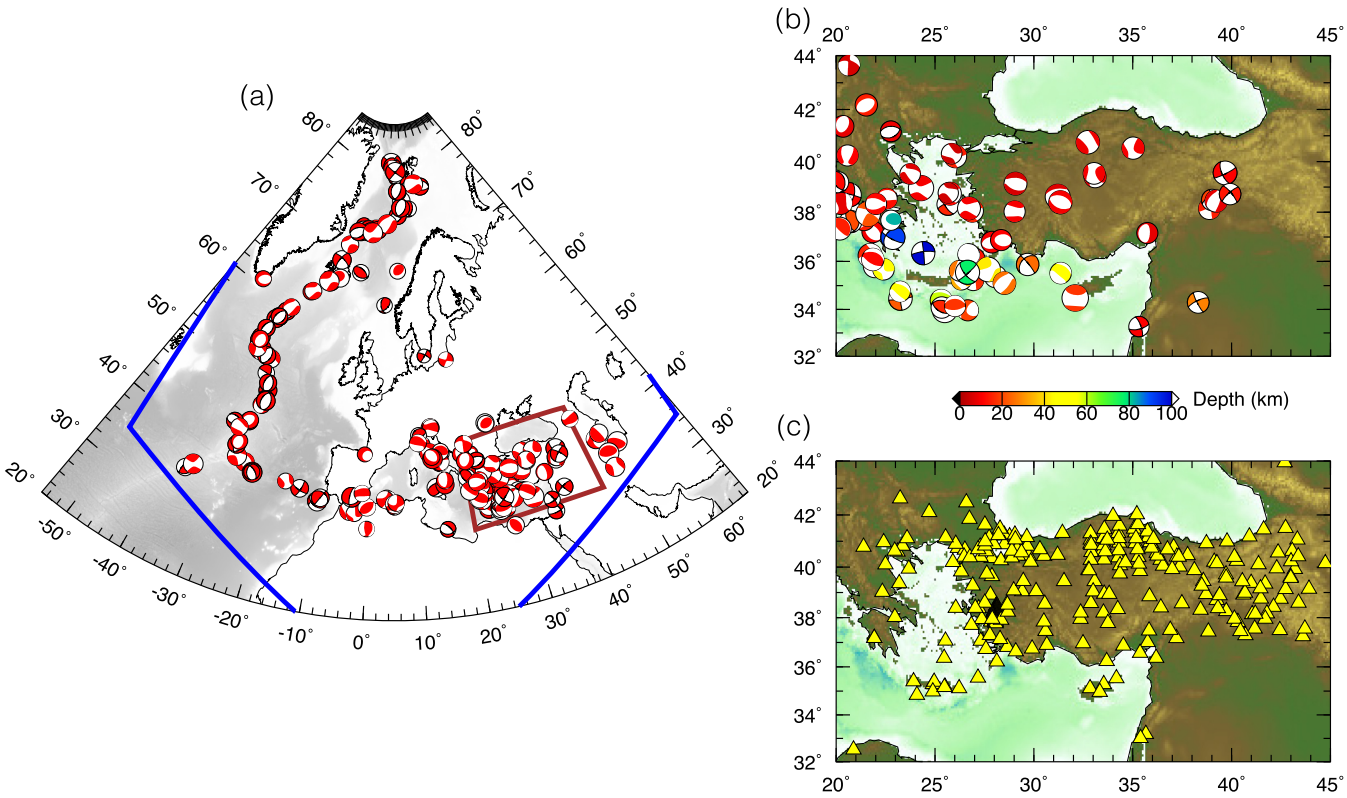

Figure 2. Distributions of earthquakes and stations used for the construction of model EU_{60}. Panel (a) shows the distribution of 190 earthquakes used in the inversion. Panel (b) shows the location of earthquakes in Anatolia, colour represents the depths of earthquakes. Panel (c) shows the distribution of seismographic stations in Anatolia and Aegean used in the inversion.

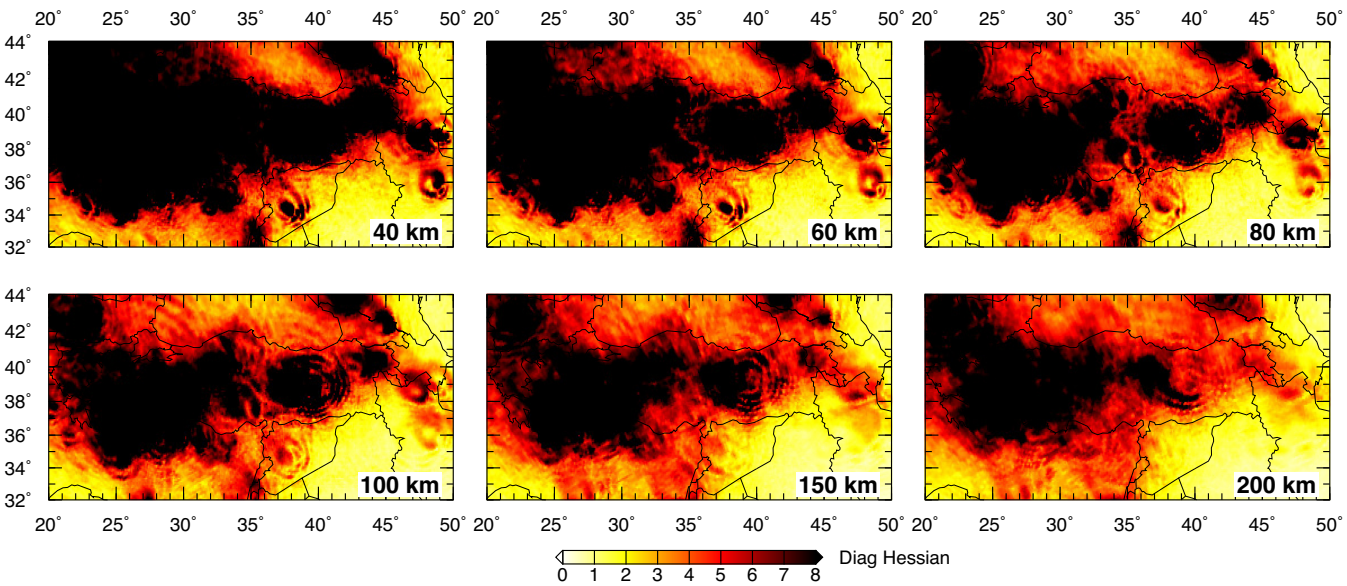

Figure 3. Horizontal cross-sections of the approximated diagonal Hessian at depths ranging from 40 to 200 km. The diagonal Hessian reflects ray density coverage for the inversion. Warm colour suggests good resolution in comparison with cool colour.

2 PREVIOUS SEISMIC STUDIES

To date, the crust and upper-mantle structures of the Anatolian Plate have been investigated using a variety of seismic techniques. For instance, large scale earthquake tomographic models (Spakman *et al.* 1993; Piromallo & Morelli 2003) suggested the Anatolian upper mantle is dominated by prominent slow wave speed anomalies. These upper-mantle features were refined later by regional body wave tomography (Lei & Zhao 2007; Biryol *et al.* 2011). For instance, slab break off was identified beneath the Cyprean Trench and the EAP. Hot asthenosphere was observed rising to the base of the lithosphere (Biryol *et al.* 2011), which might be induced

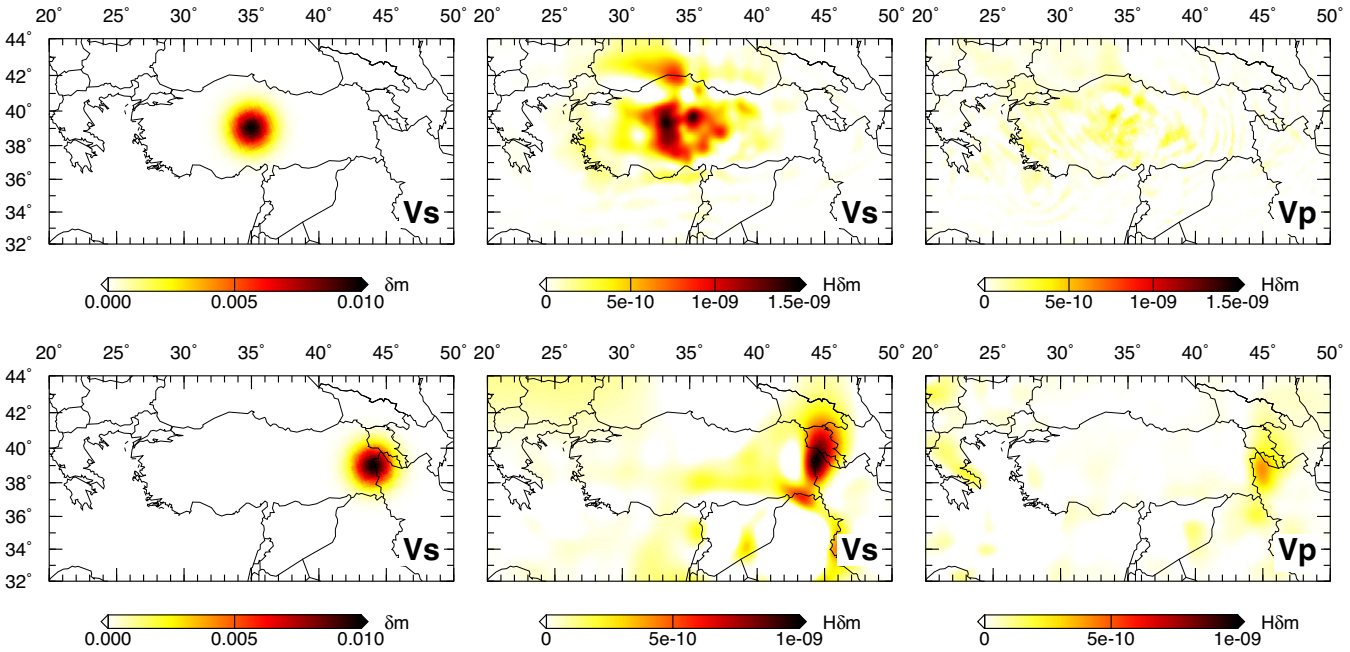

Figure 4. Point-spread functions at the Central (top) and Eastern Anatolia (bottom). Left panels show input perturbations in *Vs*. Middle and right panels are point-spread functions for *Vs* and *Vp*, respectively.

by the slab break off. Fichtner *et al.* (2013) used waveform inversion to investigate crustal and mantle signatures related to the NAF. Their results suggested that the rheologically weak fault zone might extend down to the base of the lithosphere.

The crustal structure of the Anatolian Plate has been explored using *Pn* tomography (Hearn & Ni 1994; Al-Lazki *et al.* 2003; Gans *et al.* 2009), local earthquake tomography (Koulakov *et al.* 2010), receiver functions (Zor *et al.* 2003; Vanacore *et al.* 2013), refraction profiles (Karabulut *et al.* 2003) and ambient noise tomography (Warren *et al.* 2013; Delph *et al.* 2015). Overall, the Anatolian crust is characterized by slow *Vs* anomalies (Delph *et al.* 2015). A sharp wave speed contrast across the Central Anatolian Fault Zone (CAFZ) was identified in both *Pn* (Gans *et al.* 2009) and ambient noise tomographic models (Warren *et al.* 2013). Based on receiver function analysis, Vanacore *et al.* (2013) reported elevated *Vp*/*Vs* ratio beneath the Anatolian volcanic regions. Gök *et al.* (2000) observed highly attenuated *Sn* and *Lg* phases across the EAP, which were used to infer the rheology of the lithospheric mantle. Normal Moho depth and slow crustal wave speed anomalies were observed beneath the EAP from both *Pn* and receiver function analysis (Al-Lazki *et al.* 2003; Zor *et al.* 2003), which were used to distinguish among different geodynamics models for the high elevation and negative Bouguer gravity anomalies of the EAP (McKenzie 1972; Dewey *et al.* 1986).

3 DATA AND METHODS

EU_{60} is a 3-D crust and upper-mantle model for the European continent (Zhu *et al.* 2015), constructed based on adjoint tomography (Tromp *et al.* 2005; Tape *et al.* 2009, 2010; Liu & Gu 2012). One 'cubed sphere' chunk of a global mesh (Komatitsch & Tromp 2002) is used for the development of model EU_{60}. The total number of elements is 4 692 600, and the average spacing between Gauss–Lobatto–Legendre (GLL) interpolation points is around 10 km on the Earth's surface. The minimum period can be resolved by a forward calculation is around 12 s. EPcrust (Molinari & Morelli 2011), a European crustal model with $0.5^o \times 0.5^o$ resolution, is chosen as the starting crustal model. S362ANI (Kustowski *et al.* 2008), a global radially anisotropic shear wave speed model, is chosen as the 3-D starting mantle model. Both crustal and mantle structures are simultaneously updated during the inversion, allowing us to avoid the crustal corrections (Lekic *et al.* 2010; Panning *et al.* 2010) and minimize trade-offs between crustal and upper-mantle signatures.

60 pre-conditioned conjugate gradient (Fletcher & Reeves 1964) iterations were used to constrain 3-D variations in elastic wave speeds, anelastic attenuation and azimuthal anisotropy beneath Europe. 190 earthquakes and 745 seismographic stations were utilized to illuminate the study region (Fig. 2), producing 123 919 frequency-dependent measurements. Of these stations, 101 stations were collected from the Kandilli Observatory network, which comprised the major data set for constraining the crust and upper-mantle structures of the Anatolian Plate. In the inversion, three-component, short-period body waves and long-period surface waves were combined to simultaneously constrain deep and shallow structures. A three-stage inversion strategy was used during the construction of model EU_{60}. In stage one, only frequency-dependent phase differences between observations and predications were utilized to invert for radially anisotropic model parameters, including horizontally propagated, vertically and horizontally polarized shear wave speeds (Zhu *et al.* 2012a,b). In stage two, both phase and amplitude measurements were combined to simultaneously constrain elastic wave speeds and anealstic attenuation (Zhu *et al.* 2013). In stage three, we only used three-component, long-period surface waves (25–100 s) to map azimuthally anisotropic variations at depths shallower than 250 km (Zhu & Tromp 2013). Details about the design and evolution of misfits as well as improvements on phase and amplitude measurements can be found in Zhu *et al.* (2015).

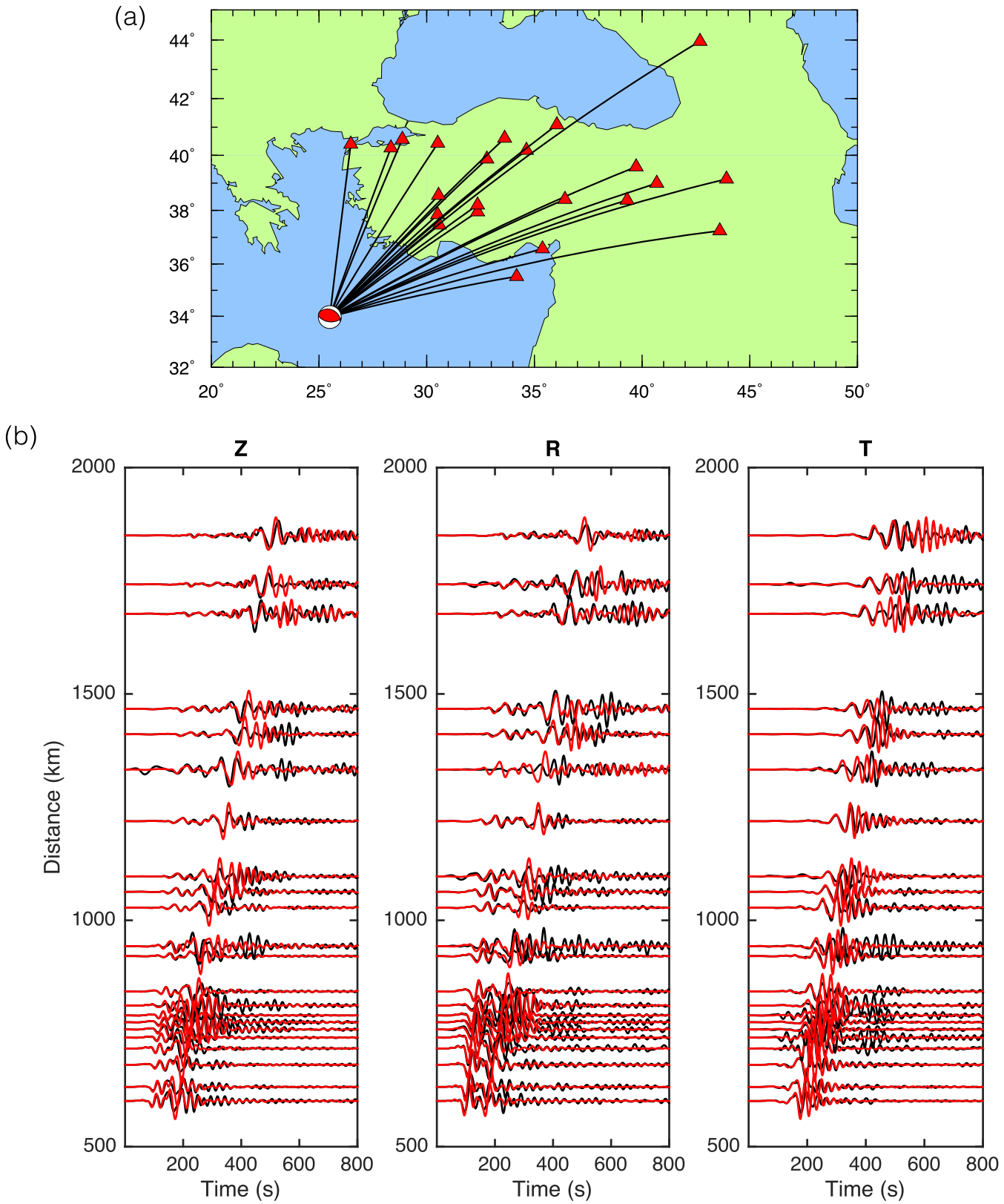

Figure 5. Comparisons for three-component, observed (black) and predicted (red) seismograms for a magnitude 6.1 earthquake occurred at a depth of 14.6 km beneath the Aegean Trench. Panel (a) shows the distribution of earthquake and stations used in comparisons. Panel (b) compares vertical (left), radial (middle) and transverse (right) component seismograms, which are arranged according to epicentre distances.

Fig. 3 presents several horizontal cross-sections of the approximated diagonal Hessian, that is, the second derivative of the misfit with respect to *Vs*, from 40 to 200 km around Aegean and Anatolia. The approximated diagonal Hessian is computed using cross-correlations between forward and adjoint acceleration wavefields (Luo *et al.* 2013). It is a good proxy for analysing ray density coverage. With the current distributions of earthquakes and stations (Fig 2), there is a relatively good data coverage for the entire Anatolian Plate at depths shallower than 200 km. To further investigate the resolution of model EU_{60} in Anatolia and analyse potential trade-offs between *Vp* and *Vs*, I compute point-spread functions at 80 km depth for the Central and Eastern Anatolia (Fig. 4). The point-spread function represents a sampled column of the Hessian matrix at a specific location, which can be computed using a finite difference approximation (Zhu *et al.* 2016). In these two examples, a Gaussian anomaly with half width about 100 km and 1 per cent perturbation is used as an input *Vs* perturbation. I compute the action of the Hessian with this input anomaly for both *Vp* and *Vs*. The computed point-spread functions for the Central and Eastern Anatolia are shown in Fig. 4. There is relatively good resolution for the Central and Eastern Anatolia. Trade-offs between *Vp* and *Vs* are relatively weak since there are small leakages from *Vs* to *Vp*. These tests suggest the robustness of *Vp*/*Vs* features in model EU_{60} for the Anatolian Plate.

Furthermore, in Fig. 5, I compare three-component, observed and predicted seismograms from model EU_{60} for a magnitude 6.1 earthquake at a depth of 14.6 km beneath the Aegean Trench (CMTSOLUTION_200907010930A). Seismograms from 22 stations are selected in this comparison, which are sorted based on their epicentre distances and filtered between 25 and 100 s. Predicted seismograms from the current model EU_{60} can fit most observed *P* and *S* waves, as well as Rayleigh and Love waves. There are still some mismatches between observations and predictions, especially for long distance, transverse component Love waves. These remaining residuals might come from the underestimation of radial anisotropy and can be utilized as input data for future regional scale investigations.

4 RESULTS

In Fig. 6, I compare relative perturbations in *Vs* (left) and the absolute values of *Vp*/*Vs* ratio (right) for the Anatolian Plate in model EU_{60}. 1-D starting model STW105 is used as the reference model to calculate these relative perturbations. The average values of isotropic *Vs* in model EU_{60} at depths ranging from 60 to 200 km are consistent with global means 4.4–4.5 km s^{-1} from models IASP91 and AK135 (Kennett & Engdahl 1991; Kennet *et al.* 1995). They are slightly higher than the estimate of 4.2–4.3 km s^{-1} from Fichtner *et al.* (2013). This disagreement might come from different treatments of shear attenuation during inversion and modeling. Global average *Vp*/*Vs* ratio is 1.74 within the crust and 1.79 within the uppermost mantle (Kennet *et al.* 1995), which are consistent with results in Fig. 6. More horizontal cross-sections for *Vp*, *Vs* and *Vp*/*Vs* ratio from 20 to 200 km can be found in Supplementary Information Fig. S1– S3. Horizontal comparisons of *Vs* and *Vp*/*Vs* ratio for the starting model S362ANI (Kustowski *et al.* 2008) can be found in Supplementary Information Fig. S10.

At shallow depths (40 and 60 km), localized slow *Vs* anomalies are observed beneath volcanoes in the Central Anatolia, including the CAVF and KAIVF. In addition, very prominent slow *Vs* anomalies (around −10 to −15 per cent) are mapped beneath the EAP and KTJ. A band feature with slow *Vs* extends from east to west along the NAF at these depths. This slow band feature is bounded to the north by the Istanbul and Sakarya zones, which are characterized by fast anomalies. Overall, there is an absence of strong wave speed contrast across the NAF, which is consistent with observations from *Pn* tomography (Gans *et al.* 2009).

An intriguing observation at shallow depths is the negative correlation between high *Vp*/*Vs* ratio with slow *Vs* anomalies beneath volcanoes and fault zones. For instance, at 60 km, the EAP and CAVF are characterized by high *Vp*/*Vs* ratio (1.9–1.95). Furthermore, along the forearc of the Aegean Trench, there is an arc like feature with localized high *Vp*/*Vs* ratio and slow *Vs* from 40 to 60 km, reflecting the volcanic arc related to the subduction of the Hellenic slab. A similar negative correlation pattern between slow Vs and high *Vp*/*Vs* ratio persists down to 100 km and dominates the entire Anatolian Plate. Regions with the slowest *Vs* (−4 to −6 per cent) and the highest *Vp*/*Vs* ratio (1.85–1.9) are still localized beneath the CAVF and EAP. In contrast, the Hellenic slab is characterized by fast *Vs* (4–6 per cent) and low *Vp*/*Vs* ratio (1.65–1.75) along the Aegean Trench. At 200 km, the magnitudes and sizes of slow *Vs* and high *Vp*/*Vs* anomalies reduce significantly in comparison with shallower depths.

In Figs 7 and 8, I present *Vs* and *Vp*/*Vs* for several vertical cross-sections across the Anatolian Plate. The west portion of the cross-section A-a corresponds to the Hellenic slab with fast *Vs* and low *Vp*/*Vs* ratio. To the east of the Hellenic slab, there is a vertical slow anomaly (−3 per cent) with high *Vp*/*Vs* ratio (around 1.9) ascending from 200 km to the surface. The location of this anomaly suggests its relation to the CAVF. The eastern part of A-a (44°E–48°E) involves anomalies with slow *Vs* and high *Vp*/*Vs* ratio, which are related to the KTJ. In cross-section B-b, the entire Anatolian Plate is dominated by pronounced slow *Vs* (−3 to −15 per cent) and elevated *Vp*/*Vs* ratio (1.83–1.95) at depths shallower than 200 km. The slowest *Vs* (<−6 per cent) and the highest *Vp*/*Vs* ratio (>1.89) are imaged beneath the KAIVF, CAVF and EAP.

Vertical cross-sections E-e to H-h are selected along the subduction strikes of the Hellenic and African slabs (Fig. 8). In cross-section E-e, the Hellenic slab is imaged subducting towards north, which is characterized by fast *Vs* (6–8 per cent) and low *Vp*/*Vs* ratio (around 1.7). The mantle wedge above the slab is characterized by slow *Vs* (−3 per cent) and high *Vp*/*Vs* ratio (1.86). It might be caused by partial melt induced by the dehydration of sediments and oceanic crust during subduction (Maruyama & Okamoto 2007). An anomaly beneath the CAVF can be easily identified in vertical cross-section F-f, where a vertical upwelling with large 'volcanic head' at shallow depths is imaged down to 150 km. In cross-sections G-g and H-h, massive anomalies with slow *Vs* (−6 per cent) and high *Vp*/*Vs* ratio (1.86–1.95) are mapped beneath the EAP from surface to 200 km. More vertical cross-sections for *Vp*, *Vs* and *Vp*/*Vs* ratio across the Anatolian Plate can be found in Supplementary Information Figs S4–S9. Similar cross-sections for the starting model S362ANI can be found in Supplementary Information Figs S11–S12.

5 MODEL INTERPRETATION

Prominent slow *Vs* anomalies at 40 and 60 km in the Central Anatolia (Fig. 6) correlate with the locations of a number of Neogene–Quaternary volcanoes in Turkey, Armenia, Azerbaijan and Geogia (Fig. 1b). Similar slow apparent *Pn* wave speeds (<7.8 km s^{-1}) were observed in the uppermost mantle beneath the Central and Eastern

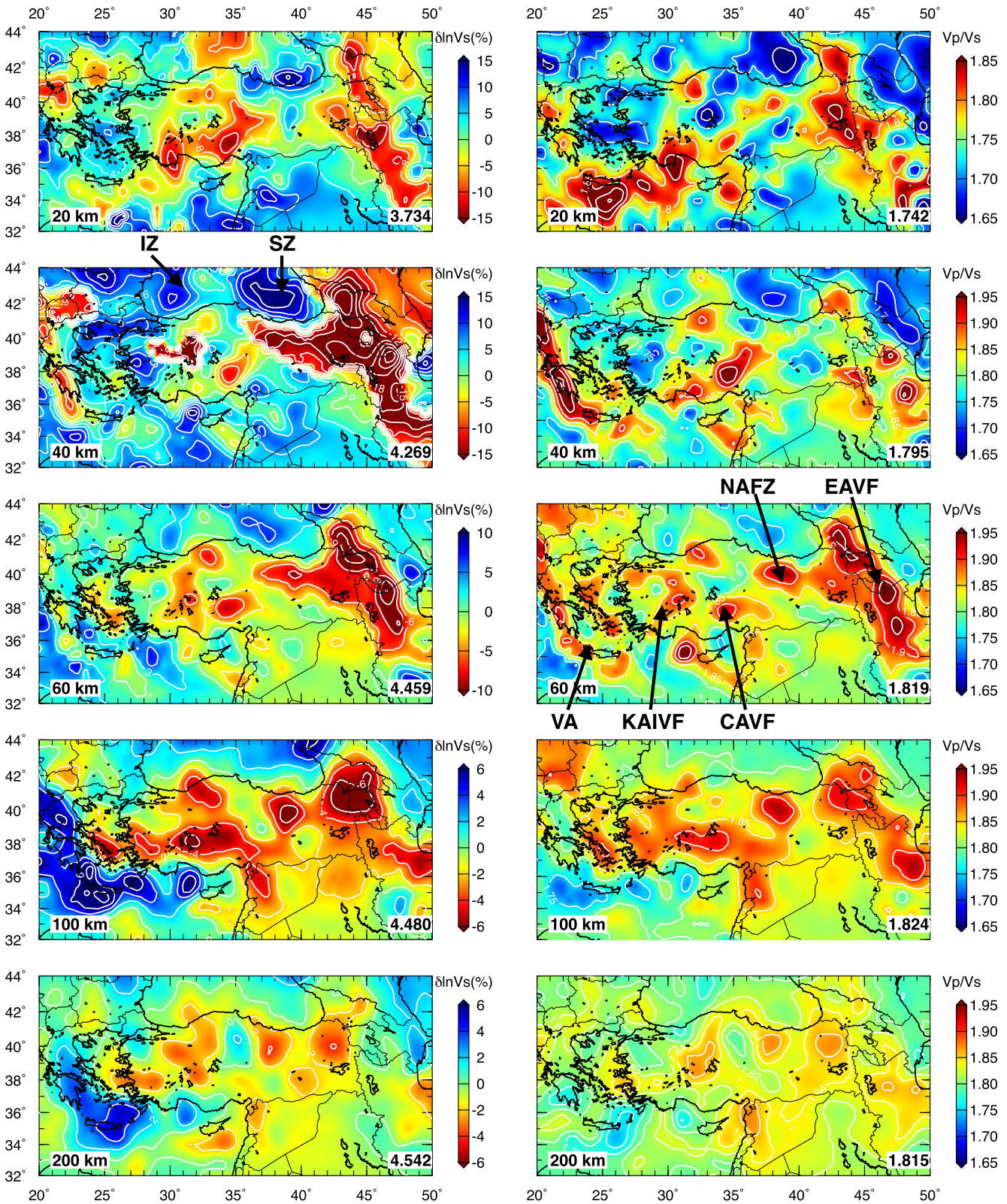

Figure 6. Horizontal cross-sections of relative perturbations in *Vs* (left) and absolute values of *Vp*/*Vs* ratio (right) for model EU_{60} at 20, 40, 60, 100 and 200 km. White lines are iso-value contours for *Vs* and *Vp*/*Vs* ratio. Average isotropic *Vs* at different depths are used as references to calculate relative perturbations. Numbers on the right bottom sides are the average *Vs* and *Vp*/*Vs* ratio at each depth.

Anatolia (Al-Lazki *et al.* 2003; Gans *et al.* 2009), which were interpreted as the presence of partial melt beneath these regions. By analysing waveform signals, Gök *et al.* (2000) observed highly attenuated *Sn* and *Lg* phases for ray paths across volcanic regions in

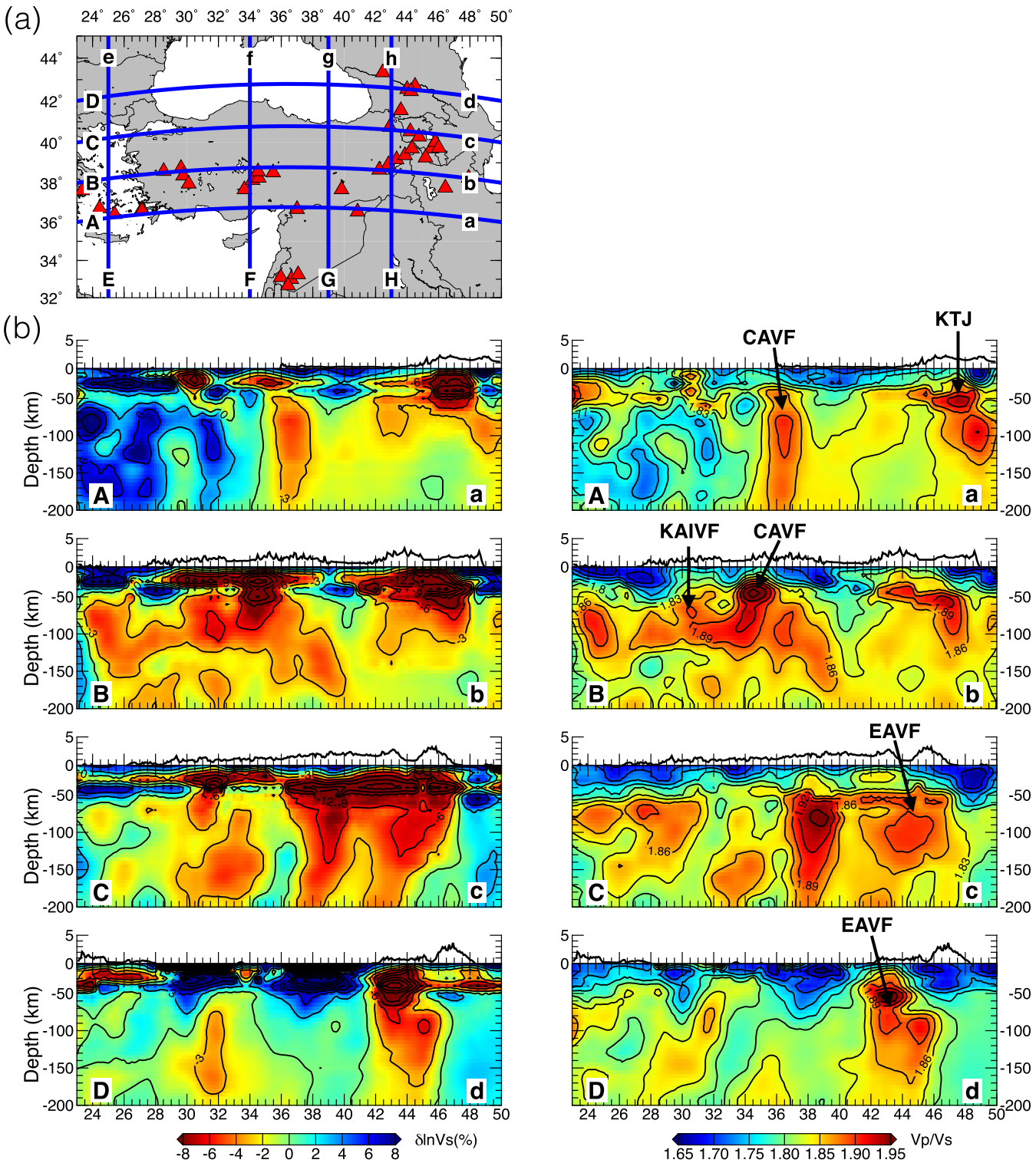

Figure 7. Vertical cross-sections of relative perturbations in *Vs* (left) and absolute values of *Vp*/*Vs* ratio (right) for model EU_{60}. Panel (a) shows the locations of these vertical cross sections. Red triangles denote Neogene–Quaternary volcanoes in Anatolia. Panel (b) presents vertical cross-sections A-a–D-d. Topographic variations from ETOPO1 (https://www.ngdc.noaa.gov/mgg/global/) are shown on top of each vertical cross-section.

the EAP. Receiver functions also revealed the presence of low wave speed anomalies in the EAP (Zor *et al.* 2003). Since normal crustal thickness (45 km) was report for the EAP (Zor *et al.* 2003), its high elevation (2 km) and negative Bouguer gravity anomalies (−100 to −150 mgl) might reflect slow wave speed anomalies within the mantle lithosphere. In addition, the slow band feature at 40 and 60 km might be indicative of rheologically weak materials within the fault zone, induced by the strike-slip motion of the NAF over the past 5–10 Myr (Fichtner *et al.* 2013).

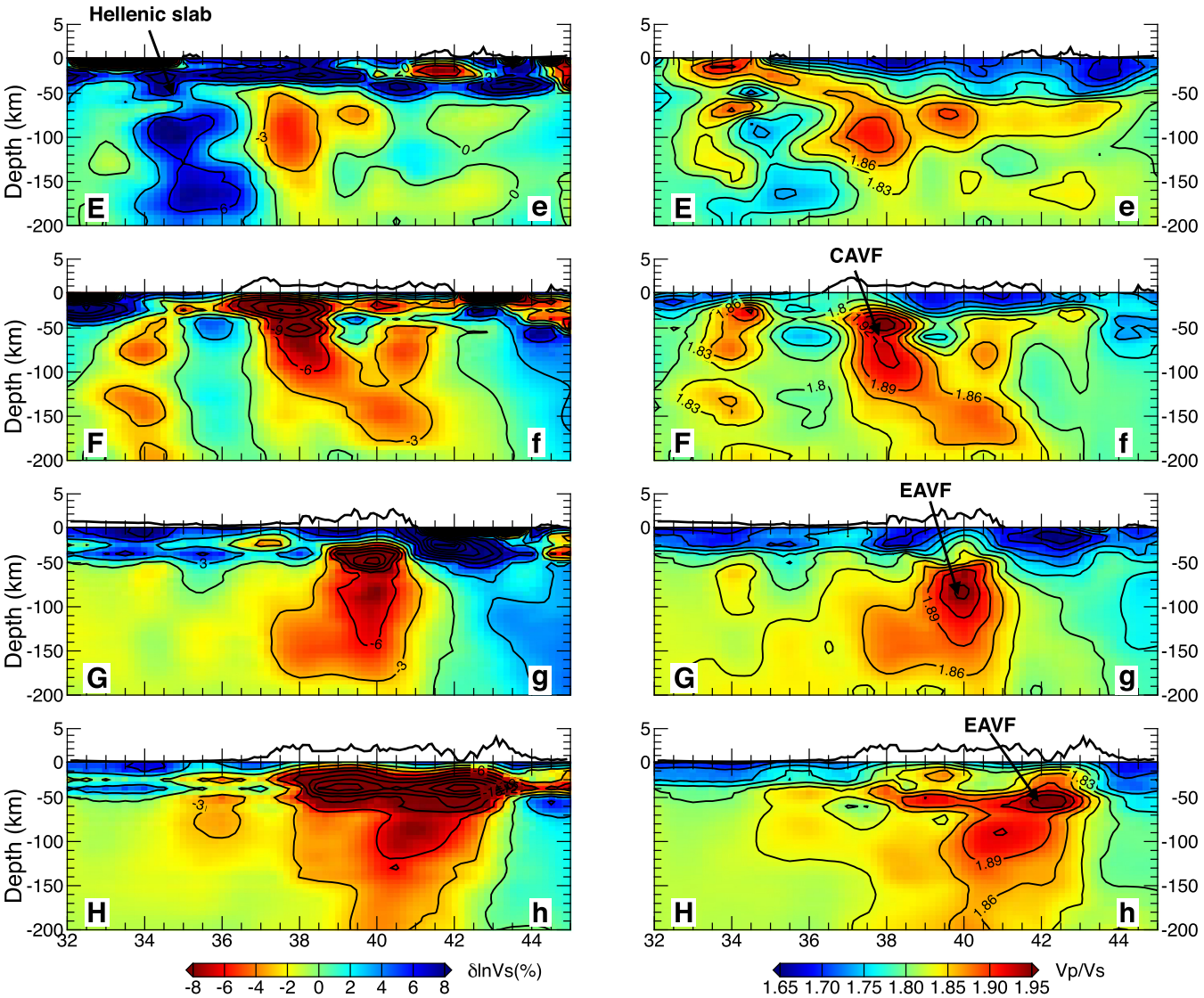

Figure 8. The same setting as Fig. 7 except for vertical cross-sections E-e–H-h.

The negative correlation between slow *Vs* and high *Vp*/*Vs* ratio at 60 km (Fig. 6) is consistent with previous receiver function analysis (Vanacore *et al.* 2013), which also reported high *Vp*/*Vs* ratio (>1.85) around the Moho depth beneath these regions. Slow *Vs* combined with high *Vp*/*Vs* ratio might be indicative of partial melt in these areas (see the Section 6). The observations of slow *Vs* and high *Vp*/*Vs* ratio beneath the KAIVF, CAVF and EAP (vertical cross-sections B-b in Fig. 7, and F-f, H-h in Fig. 8) suggest that there might be massive magma supports for volcanoes in the Central and Eastern Anatolia. In vertical cross-section C-c and D-d, the volcanoes in the EAP are characterized by prominent slow *Vs* and high *Vp*/*Vs* ratio, which might relate to the uplift of the EAP.

6 DISCUSSION

Based on the horizontal and vertical cross-sections in Figs 6–8, I find a negative correlation between *Vs* and *Vp*/*Vs* ratio beneath volcanic fields in Anatolia. The magnitudes of slow *Vs* beneath volcanoes are so large (−6 to −15 per cent) that temperature and composition should play important roles. In particular, partial melt may be an important contribution considering high *Vp*/*Vs* ratio (1.85–1.95) in comparison with global average values (1.74–1.79; Kennet *et al.* 1995).

To further analyse the correlation between *Vs* and *Vp*/*Vs* ratio and diagnose the presence of partial melt, in Fig. 9, I plot relative perturbations in *Vp* and *Vs* for model grid points associated with volcanic and non-volcanic regions. The volcanic model grid points are selected based on the locations of volcanic centres shown in Fig. 1(b). For instance, GLL points within a radius of 100 km around the volcanic centres are considered as the volcanic model grid points. The crustal thickness in EPcrust (Molinari & Morelli 2011) is shown in Fig. 1(d), which ranges from 40 to 60 km in Anatolia. The linear fitting slope of $\delta \ln Vs/\delta \ln V_p$ should be around 1.2–2 if the physical cause of velocity variations mainly comes from temperature (Anderson *et al.* 1992; Goes *et al.* 2000).

At shallower depths (50–60 km), the linear regression slopes of $\delta \ln V_s/\delta \ln V_p$ for non-volcanic grid points are around 1.49–1.71, which are slightly lower than the measurements of the western US (1.8) from Schmandt & Humphreys (2010). But they are consistent with theoretical prediction for thermal variations (1.6). The slopes of volcanic grid points are greater than 2.24 and some samples

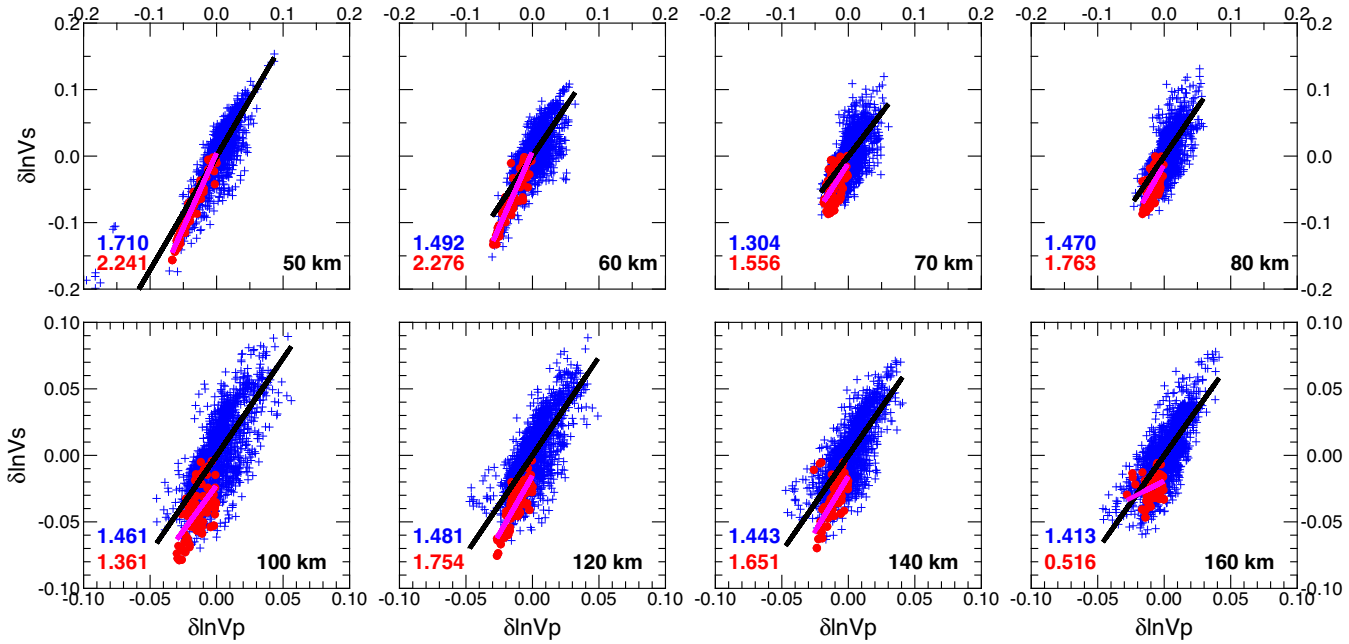

Figure 9. 2-D correlation diagrams for $\delta\ln V_s$ and $\delta\ln V_p$ at different depths. Different panels show correlations between $\delta\ln V_s$ and $\delta\ln V_p$ from 50 to 160 km. Blue crosses are samples for non-volcanic areas and red dots are samples from volcanic provinces. Magenta and black lines are the best linear fits for volcanic and non-volcanic samples, respectively. Red and blue numbers on the bottom left side of each panel are the linear regression slopes of $\delta\ln V_s/\delta\ln V_p$ for volcanic and non-volcanic samples, respectively.

involve *Vs* slower than −10 per cent, suggesting the presence of partial melt (Hammond & Humphreys 2000). A similar steep slope (2.33) has been reported beneath Yellowstone and the Snake River Plain in the western US (Schmandt & Humphreys 2010).

Below the Moho (greater than 60 km in Fig. 1d), the slopes of $\delta\ln V_s/\delta\ln V_p$ for both volcanic and non-volcanic grid points are reduced. For instance, the slope of the non-volcanic samples reduces to normal values around 1.44–1.49, and the volcanic samples still involve relatively steep slopes around 1.7. Decompression induced partial melt during the ascent of mantle might be the major cause of these observations.

In Fig. 10, I compare *Vp* and *Vp*/*Vs* in model EU_{60} with theoretical single-phase calculations from Yamamoto *et al.* (1981) and Nakajima *et al.* (2001). Their method computes effective elastic constants for a composite with cracks filled with different volume fractions of melt (0–10 per cent). In their cases, the melt is distributed in randomly oriented spheroidal inclusion with a specified aspect ratio. Three different aspect ratios (0.001, 0.01 and 0.1) were taken into account in their computations. In this paper, I only compare results at 20, 40 and 60 km, representing the upper crust, lower crust and uppermost mantle of the Anatolian Plate, respectively. Samples from volcanic regions are shown as solid stars in Fig. 10. Within the upper crust (Figs 10 a and b), tomographic results follow the melt curve with aspect ratio of 0.1. The volume fraction curve suggests the presence of 4-6 per cent of melt accumulation within the upper crust. In the lower crust (Figs 10 c and d), tomographic results suggest the presence of cracks with aspect ratio of 0.01, which are filled with about 2 per cent melt. In the uppermost mantle (Figs 10 e and f), estimated *Vp*/*Vs* ratios (around 1.85–2) from model EU_{60} are higher than theoretical calculations, which might suggest the presence of cracks with aspect ratio smaller than 0.001. From the volume fraction curve, there is a relatively small amount of melt in the uppermost mantle beneath the Anatolian volcanic fields (<1 per cent). These comparisons are just a first-order approximation since other effects, including temperature and porosity, have not been taken into account in the theoretical computations (Nakajima *et al.* 2001). In addition, only a single-phase case (melt) is discussed, other factors, such as water and multiphase situation, may affect above interpretations.

7 CONCLUSION

In this paper, I analyse *Vp*, *Vs* and *Vp*/*Vs* results for the crust and uppermost mantle of the Anatolian Plate based on a 3-D tomographic model EU_{60}. Prominent slow *Vs* anomalies (−6 to −15 per cent) are observed beneath volcanoes in the Central and Eastern Anatolia. The magnitudes of these slow anomalies are so large that temperature and composition should play important roles. An interesting observation in this paper is the negative correlation between slow *Vs* and high *Vp*/*Vs* ratio (1.85–1.95) beneath the Anatolian volcanic fields. There is a distinct pattern in the linear regression slopes of relative perturbations in *Vp* and *Vs* between grid points for volcanic and non-volcanic regions. Overall, the slopes of $\delta\ln V_s/\delta\ln V_p$ are higher for volcanic grid points (1.6–2.2) in comparison with non-volcanic grid points (around 1.4). Volcanic grid points with maximum $\delta\ln V_s/\delta\ln V_p$ slopes (>2.2) are found near the Moho depth. These observations suggest the presence of melt accumulation beneath volcanoes in the Central and Eastern Anatolia. Comparisons with theoretical partial melting calculations suggest 2–6 per cent partial melt with aspect ratio around 0.1–0.01 may exist in the upper and lower crust. In the uppermost mantle, the volume fraction of melt accumulation may reduce to less than 1 per cent, and the aspect ratios of cracks may be less than 0.001.

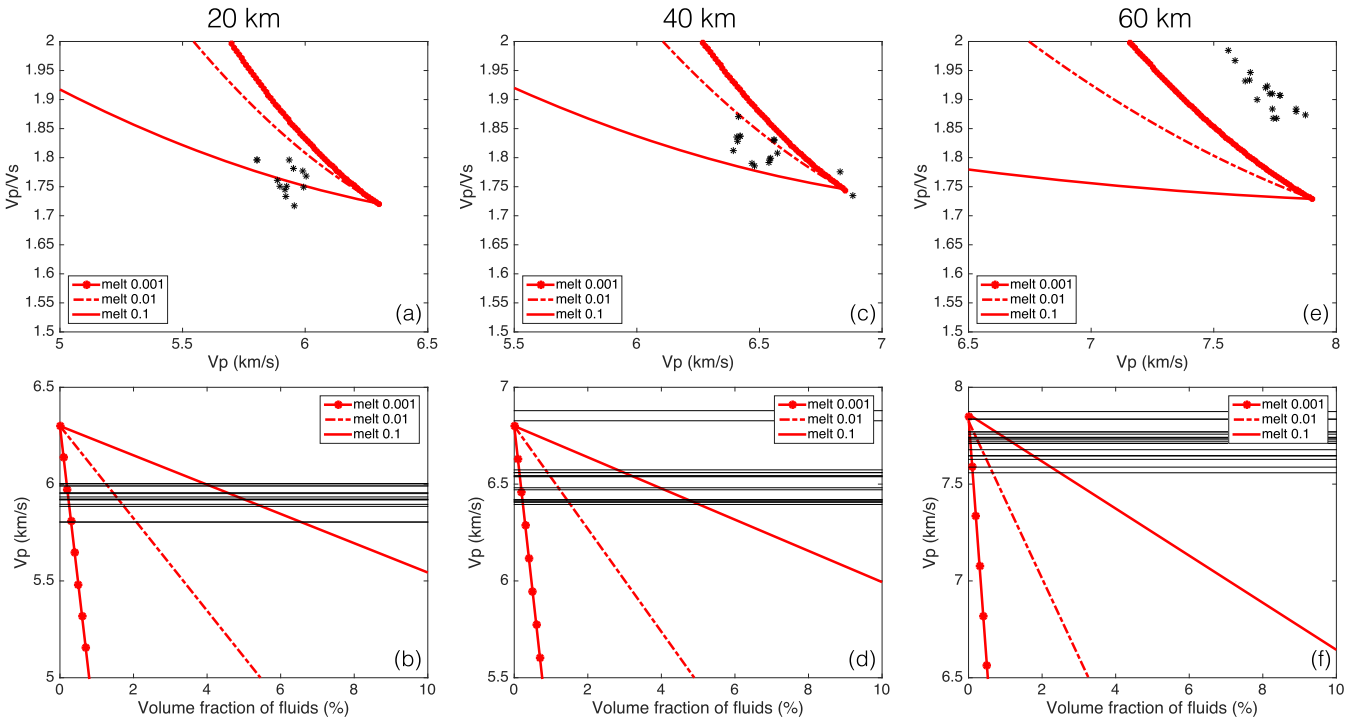

Figure 10. Comparisons between seismic observations and theoretical computations of effective *Vp* and *Vp*/*Vs* ratio for a composite with melt-filled inclusions (Yamamoto *et al.* 1981; Nakajima *et al.* 2001). Panel (a) shows correlations between *Vp* and *Vp*/*Vs* ratio for melt-filled cracks with different aspect ratios (red lines) in the upper crust. Black solid stars are observations for volcanic samples in model EU_{60} around 20 km. Panel (b) shows the variations of *Vp* with different volume fractions of melt (red lines). Black lines are *Vp* results from model EU_{60} around 20 km. Panels (c) and (d) are results for the lower crust (around 40 km). Panels (e) and (f) are results for the uppermost mantle (around 60 km).

ACKNOWLEDGEMENTS

I am grateful for the discussions with Dr Jeroen Tromp and Dr Rob Govers about the tectonics of the Anatolian Plate. I thank the editor Dr Ludovic Métivier and three anonymous reviewers for providing valuable suggestions to significantly improve the manuscript. I thank the Texas Advanced Computing Center for providing computational resources for this work. This paper is contribution no. 1328 from the Department of Geosciences at the University of Texas at Dallas.

REFERENCES

Al-Lazki, A., Seber, D., Sandvol, E., Turkelli, N., Mohamad, R. & Barazangi, M., 2003. Tomographic Pn velocity and anisotropy structure beneath the Anatolian plateau (eastern Turkey) and the surrounding regions, *Geophys. Res. Lett.,* **30,** doi:10.1029/2003GL017391.

Anderson, O., Isaak, D. & Oda, H., 1992. High-temperature elastic constant data on minearls relevant to geophysics, *Rev. Geophys.,* **30,** 57–90.

Ates, A., Kearey, P. & Tufan, S., 1999. New gravity and magnetic anomaly maps of Turkey, *Geophys. J. Int.,* **136,** 499–502.

Biryol, C., Beck, S., Zandt, G. & Özacar, A., 2011. Segmented African lithosphere beneath the Anatolian region inferred from teleseismic *P*-wave tomography, *Geophys. J. Int.,* **184,** 1037–1057.

Delph, J., Biryol, C., Beck, S., Zandt, G. & Ward, K., 2015. Shear wave velocity structure of the Anatolian plate: anomalously slow crust in southwestern Turkey, *Geophys. J. Int.,* **202,** 261–276.

Dewey, J., Hempton, M., Kidd, W., Saroglu, F. & Şengör, A., 1986. Shortening of continental lithosphere: the neotectonics of Eastern Aantolian —a young collision zone, *Geol. Soc. Lond. Spec. Pub,* **19,** 3–36.

Fichtner, A., Saygin, E., Taymaz, T., Cupillard, P., Capdeville, Y. & Trampert, J., 2013. The deep structure of the North Anatolian Fault Zone, *Earth Planet. Sci. Lett.,* **373,** 109–117.

Fletcher, R. & Reeves, C., 1964. Function minimization by conjugate gradients, *Comput. J.,* **7,** 149–154.

Gans, C., Beck, S., Zandt, G., Biryol, C. & Ozacar, A., 2009. Detecting the limit of slab break-off in central turkey: new high-resolution *Pn* tomography results, *Geophys. J. Int.,* **179,** 1566–1572.

Goes, S., Govers, R. & Vacher, P., 2000. Shallow mantle temperatures under Europe from *P* and *S* wave tomography, *J. Geophys. Res.,* **105,** 11 153–11 170.

Gök, R., Türkelli, N., Sandvol, E., Seber, D. & Barazangi, M., 2000. Regional wave propagation in Turkey and surrounding region, *Geophys. Res. Lett.,* **27,** 429–432.

Hammond, W. & Humphreys, E., 2000. Upper mantle seismic wave velocity: effects of realistic partial melt geometries, *J. Geophys. Res.,* **105,** 975–986.

Hearn, T. & Ni, J., 1994. *Pn* velocities beneath continental collision zones: the Turkish-Iranian Plateau, *Geophys. J. Int.,* **117,** 273–283.

Karabulut, H., Özalaybey, S., Taymaz, T., Aktar, M., Selvi, O. & Kocaoğlu, A., 2003. A tomographic image of the shallow crustal structure in the Eastern Marmar, *Geophys. Res. Lett.,* **30,** doi:10.1029/2003GL018074.

Kennet, B., Engdahl, E. & Buland, R., 1995. Constraints on seismic velocities in the Earth from travel times, *Geophys. J. Int.,* **122,** 108–124.

Kennett, B.L.N. & Engdahl, E.R., 1991. Traveltimes for global earthquake location and phase identification, *Geophys. J. Int.,* **105,** 429–465.

Komatitsch, D. & Tromp, J., 2002. Spectral-element simulations of global seismic wave propagation—I. Validataion, *Geophys. J. Int.,* **149,** 390–412.

Koulakov, I., Bindi, D., Parolai, S., Grosser, H. & Milkereit, C., 2010. Distribution of seismic velocities and attenuation in the crust beneath the North Anatolian Fault (Turkey) from local earthquake tomography, *Bull. Seism. Soc. Am.,* **100,** 207–224.

Kustowski, B., Ekström, G. & Dziewonski, A., 2008. Anisotropic shear-wave velocity structure of the Earth's mantle: a global model, *J. Geophys. Res.,* **113,** B06306, doi:10.1029/2007JB005169.

Lailly, P., 1983. The seismic inverse problem as a sequence of before stack migration, in *Conference on Inverse Scattering: Theory and Application,*

pp. 206–220, ed. Bednar, J., Society for Industrial and Applied Mathematics.
Lei, J. & Zhao, D., 2007. Teleseismic evidence for a break-off subducting slab under Eastern Turkey, *Earth Planet. Sci. Lett.,* **257,** 14–28.
Lekic, V., Panning, M. & ROamnowicz, B., 2010. A simple method for improving crustal correction in waveform tomography, *Geophys. J. Int.,* **182,** 265–278.
Lin, G., Amelung, F., Shearer, P. & Okubo, P., 2015. Location and size of the shallow magma reservoir beneath Kilauea caldera, constraints from near-source *Vp*/*Vs* ratios, *Geophys. Res. Lett.,* **42,** 8349–8357.
Liu, Q. & Gu, Y., 2012. Seismic imaging: from classical to adjiont tomography, *Tectonophysics,* **566,** 31–66.
Luo, Y., Modrak, R. & Tromp, J., 2013. Strategies in adjoint tomography, in *Handbook of Geomathematics,* 2nd edn, pp. 1–52, eds Freeden, Z.N.W. & Sonar, T., Springer.
Maruyama, S. & Okamoto, K., 2007. Water transportation from the subducting slab into the mantle transition zone, *Gondwana Res.,* **11,** 148–165.
McKenzie, D., 1972. Active tectonics of the Mediterranean region, *Geophys. J. R. astr. Soc,* **30,** 109–185.
Molinari, I. & Morelli, A., 2011. EPcrust: a reference crustal model for the European Plate, *Geophys. J. Int.,* **185,** 352–364.
Nakajima, J., Matsuzawa, T., Hasegawa, A. & Zhao, D., 2001. Three-dimensional structure of Vp, Vs and Vp/Vs beneath northeastern Japan: implications for arc magmatism and fluids, *J. Geophys. Res.,* **106,** 21 843–21 857.
Ozacar, A., Gilbert, H. & Zandt, G., 2008. Upper mantle discontinuity structure beneath East Anatolian Plateau (Turkey) from receiver functions, *Earth Planet. Sci. Lett.,* **269,** 426–434.
Panning, M., Lekic, V. & Romanowicz, B., 2010. The importance of crustal corrections in the development of a new global model of radial anisotropy, *J. Geophys. Res.,* **115,** doi:10.1029/2010JB007520.
Pearce, J. *et al.*, 1990. Genesis of collision volcanism in eastern Anatolia, Turkey, *J. Volcanol. Geotherm. Res,* **44,** 219–228.
Piromallo, C. & Morelli, A., 2003. *P* wave tomography of the mantle under the Alpine-Mediterranean area, *J. Geophys. Res.,* **108,** 2065, .
Reid, M., Schleiffarth, W., Cosca, M., Delph, J., Blichert-Toft, J. & Cooper, K., 2017. Shallow melting of MORB-like mantle under hot continetal lithosphere, Central Anatolia, *Geochem. Geophys. Geosyst.,* **18,** 1866–1888.
Reilinger, R., *et al.*, 1997. Global Positioning System measurements of present-day crustal movements in the Arabia-Africa-Eurasia plate collision zone, *J. Geophys. Res.,* **102,** 9983–9999.
Sandvol, E., Seber, D., Barazangi, M., Vernon, F., Mellors, R. & Al-Amri, A., 1998. Lithospheric seismic velocity discontinuities beneath the Arabian Shield, *Geophys. Res. Lett.,* **25,** 2873–2876.
Schmandt, B. & Humphreys, E., 2010. Complex subduction and small-scale convection revealed by body-wave tomography of the western United States upper mantle, *Earth Planet. Sci. Lett.,* **297,** 435–445.
Şengör, A., Görür, N. & Şaroğlu, F., 1985. Strike-slip faulting and related basin formation in zones of tectonic escape: Turkey as a case study, in *Strike-Slip Faulting and Basin Formation,* pp. 227–264, eds Biddle, K. & Christie-Blick, N., Society of Economic Paleontologists and Mineralogists Special Publication.
Spakman, W., van der Lee, S. & van der Lee, R., 1993. Travel-time tomography of the European-Mediterranean mantle down to 1400 km, *Phys. Earth Planet. Inter.,* **79,** 3–74.
Tape, C., Liu, Q., Maggi, A. & Tromp, J., 2009. Adjoint tomography of the southern California crust, *Science,* **325,** 988–992.
Tape, C., Liu, Q., Maggi, A. & Tromp, J., 2010. Seismic tomography of the southern California crust based on spectral-element and adjoint methods, *Geophys. J. Int.,* **180,** 433–462.
Tarantola, A., 1984. Inversion of seismic reflection data in the acoustic approximation, *Geophysics,* **49,** 1259–1266.
Tromp, J., Tape, C. & Liu, Q.Y., 2005. Seismic tomography, adjoint methods, time reversal and banana-doughnut kernels, *Geophys. J. Int.,* **160,** 195–216.
Vanacore, E., Taymaz, T. & Saygin, E., 2013. Moho structure of the Anatolian plate from receiver function analysis, *Geophys. J. Int.,* **193,** 329–337.
Virieux, J. & Operto, S., 2009. An overview of full-waveform inversion in exploration geophysics, *Geophysics,* **74,** WCC1–WCC26.
Warren, L., Beck, S., Biryol, C., Zandt, G., Ozacar, A. & Yang, Y., 2013. Crustal velocity structure of Central and Eastern Turkey from ambient noise tomography, *Geophys. J. Int.,* **194,** 1941–1954.
Wortel, M.J.R. & Spakman, W., 2000. Subduction and slab detachment in the Mediterranean-Carpathian region, *Science,* **290,** 1910–1917.
Yamamoto, K., Kosuga, M. & Hirasawa, T., 1981. A theoretical method for determination of effective elastic constants of isotrophic composites, *Sci. Rep. Tohoku. Univ.,* **28,** 47–67.
Zhu, H. & Tromp, J., 2013. Mapping tectonic deformation in the crust and upper mantle beneath Europe and the North Atlantic Ocean, *Science,* **341,** 871–875.
Zhu, H., Bozdağ, E., Peter, D. & Tromp, J., 2012a. Seismic wavespeed images across the Iapetus and Tornquist suture zones, *Geophys. Res. Lett.,* **39,** L18304, doi:10.1029/2012GL053053.
Zhu, H., Bozdağ, E., Peter, D. & Tromp, J., 2012b. Structure of the European upper mantle revealed by adjoint tomography, *Nat. Geosci.,* **5,** 493–498.
Zhu, H., Bozdağ, E., Duffy, T. & Tromp, J., 2013. Seismic attenuation beneath Europe and the North Atlantic: implicitions for water in the mantle, *Earth Planet. Sci. Lett.,* **381,** 1–11.
Zhu, H., Bozdağ, E. & Tromp, J., 2015. Seismic structure of the European upper mantle based on adjoint tomography, *Geophys. J. Int.,* **201,** 18–52.
Zhu, H., Li, S., Fomel, S., Stadler, G. & Ghattas, O., 2016. A Bayesian approach to estimate uncertainty for full-waveform inversion using a priori information from depth migration, *Geophysics,* **81,** R307–R323.
Zor, E., Sandvol, E., Gürbüz, C., Turkelli, N., Seber, D. & Barazangi, M., 2003. The crustal structure of the East Anatolian plateau (Turkey) from receiver functions, *Geophys. Res. Lett.,* **30,** doi:10.1029/2003GL018192.

SUPPORTING INFORMATION

Supplementary data are available at *GJI* online.

Figure S1. Horizontal cross sections of relative perturbations in isotropic shear wavespeeds ($\delta \ln V_s$) in model EU_{60} from 20 to 200 km. Average isotropic shear wavespeeds at different depths (numbers on the right bottom sides in each panel) are used as references to calculate the relative perturbations.

Figure S2. The same setting as Fig. S1 except for relative perturbations in Vp.

Figure S3. Horizontal cross sections of $V_p = V_s$ ratio in model EU_{60} from 20 to 200 km. Numbers on the right bottom sides are average $V_p = V_s$ ratios at different depths in Anatolia.

Figure S4. Vertical cross sections of relative perturbations in isotropic shear wavespeeds ($\delta \ln V_s$) for model EU_{60}. Top left panel shows the locations of these vertical cross sections. Red triangles denote Cenozoic volcanoes in Anatolia.

Figure S5. The same setting as Fig. S4 except for relative perturbations in Vp.

Figure S6. The same setting as Fig. S4 except for $V_p = V_s$ ratio.

Figure S7. Vertical cross sections of relative perturbations in isotropic shear wavespeeds ($\delta \ln V_s$) for model EU_{60}. Top left panel shows the locations of these vertical cross sections. Red triangles denote Cenozoic volcanoes in Anatolia.

Figure S8. The same setting as Fig. S7 except for relative perturbations in Vp.

Figure S9. The same setting as Fig. S7 except for $V_p = V_s$ ratio.

Figure S10. Horizontal cross sections of relative perturbations in Vs (left) and absolute values of Vp/Vs ratio (right) for the starting model at 20, 40, 60, 100 and 200 km (in comparison with Fig. 6 in the main text).

Figure S11. Vertical cross sections of relative perturbations in Vs (left) and absolute values of Vp/Vs ratio (right) for the starting model (in comparison with Fig. 7 in the main text).

Figure S12. The same setting as Fig. S11 except for vertical cross sections E-e to H-h (in comparison with Fig. 8 in the main text).

Please note: Oxford University Press is not responsible for the content or functionality of any supporting materials supplied by the authors. Any queries (other than missing material) should be directed to the corresponding author for the article.